Microscopic Mechanisms, Morphology and Defects Formation in the Thermally Activated Crystallization of Methylammonium Lead Iodide

Simone Argiolas,[†,‡] Claudia Caddeo,[†] Christian Tantardini,[†] Jgor Pensè Schone,[†]
David Dell'Angelo,[‡,†] Alessio Filippetti,[‡,†] and Alessandro Mattoni[*,†]

†*CNR - Istituto Officina dei Materiali (IOM) Cagliari, Cittadella Universitaria, Monserrato (CA), 09042, Italy*
‡*Dipartimento di Fisica, Università degli Studi di Cagliari, Cittadella Universitaria, Monserrato (CA), 09042, Italy*

E-mail: mattoni@iom.cnr.it

Abstract

In this study, we unravel the atomistic mechanisms that govern the crystallization process of methylammonium lead iodide through the application of microsecond timescale molecular dynamics simulations.

The findings indicate that methylammonium iodide (MAI) and lead iodide (PbI_2) precursors exhibit a propensity to aggregate into a disordered film, which ultimately undergoes a thermally activated disorder-to-order transformation to achieve crystallization. Notably, the crystal evolution during the annealing process reveals morphological characteristics consistent with the Straski-Krastanov growth mode.

The temperature dependence of the crystal growth rate demonstrates an activation energy of 0.37 eV, which may be ascribed to the energy required to dissociate defective Pb-I bonds and facilitate Pb diffusion. Finally, the mechanisms underlying the spontaneous generation of lead vacancies are examined, suggesting a kinetic origin for such optically active defects. In principle, the latter suggests the potential for reducing their concentration through the optimization of growth parameters.

Keywords

hybrid perovskites; crystallization; molecular dynamics; ionic diffusion; ionic defects

Introduction

Methylammonium lead iodide (MAPI) was first synthesized and characterized in 1978 by Weber[1] and is the most important example of an organic/inorganic hybrid crystal with ABX_3 perovskite structure.[2–4] The positively charged molecular cations (MA) have a large enough volume to fill the sites among the PbI_6 octahedra network, giving rise to a tetragonal crystal. All-inorganic perovskites, such as $CsPbI_3$, have superior thermal stability[5] but suffer from poor phase stability at room temperature[6] and easily tend to transform into non-perovskite δ-phases.[7] After some initial applications of MAPI as an optoelectronic material[8] and as sensitizer in titanium-based Gratzel cells,[9] MAPI has become the protagonist of hybrid photovoltaic technology and the reference active layer semiconductor of perovskite solar cells. Beside MAPI, formamidinium lead iodide ($FAPbI_3$) exhibits application prospects due to high thermal stability and optoelectronic properties,[10] while phase instability and scalability need to be addressed for broader application.[11]

The integration of multiple cations in the perovskite structure (*e.g.* alloying FA, MA with other elements like cesium) allows for fine-tuning of the material properties, improving surface morphology and carrier lifetimes[12] leading to improvements in solar cell performance. The power conversion efficiency of hybrid perovskites have surpassed recently 26% in single junctions[13,14] and 31% in tandem architectures.[15] Given the large combination of molecules, metals, and halogen atoms, along with the presence of several low-dimensional phases, the class of hybrid perovskites shows great design flexibility and a huge potential ranging from energy and optoelectronic devices,[16] to thermoelectricity, spintronics and many others.[17–21]

The present study focuses on MAPI as the prototypical example of the class of hybrid perovskite crystals. The outstanding performances of MAPI are undoubtedly due to the exceptional semiconducting properties of this crystal,[22–24] including its high optical absorption coefficient in the visible range, high electron mobility[25–28] , and remarkable resilience to defects.[29] Despite high photoconversion efficiencies, perovskite solar cells suffer from low thermal,[30] and chemical stability[31–33] that limit their lifetime under typical operating conditions. These problems become even more critical when attempting to replace toxic cations (Pb) with non-toxic alternatives such as Sn, due to its tendency to oxidize.[34–36]

The impressive advancement of this photovoltaic technology has been made possible by the development of chemical methods of crystal growth in solution[37,38] (*e.g.* spin-coating[39]) that have undoubtedly contributed to the success and diffusion of this technology in terms of its cost-effectiveness and simplicity. However, solution-based synthesis makes use of hazardous solvents[40,41] and faces limitations in achieving atomic-scale control while simultaneously fulfilling the requirements for extensive-area synthesis.[42]

The significance of the synthesis and the mechanisms of crystal growth to improve the perovksite properties have been underscored by several works that have studied, for example, the formation of perovskite from precursors[43] or the nucleation in γ-butyrolactone solution.[44] Other studies have explored the role of solvent annealing and humidity in enhancing crystal growth,[45] the advantages of thermal evaporation[46] or vapor-assisted deposition methods in achieving high-quality and more stable films.[47] In recent years, a growing of studies have been based on vacuum synthesis techniques (*e.g.* chemical vapour deposition,[48] sputtering,[49] thermal evaporation,[46,47,50] molecular beam epitaxy[51]) without the use of solvents and additives. The dominant thermal evaporation technique[52] is the multisource evaporation,[53] in which each precursor is coevaporated along with all other precursors (*e.g.* PbI_2 and MAI salts) to form the perovskite layer. Thermal evaporation has advantages over solution-processing, including film uniformity[54] and conformal growth,[55] low material consumption, a lack of toxic solvents, reproducibility and scalability.[54]

However, it is a formidable challenge to achieve an in-depth understanding and control of growth mechanisms and morphology during evaporation, as this would require a comprehensive *in situ* monitoring and ex situ characterization. As a result, many fundamental properties of MAPI crystal growth remain unknown, including ionic diffusivities, disorder, activation energies, mechanisms of defects formation, and, more importantly, the attribution of the intrinsic growth mechanisms of MAPI to any of the well-known modes, such as layer growth (Frank–van der Merwe), island growth (Volmer-Weber), or layer-island growth (Stranski–Krastanov).[56,57] The Frank–van der Merwe is a layer-by-layer growth mode in which, preferentially, a crystal layer tends to be completed before a new layer is started above it. The Volmer–Weber, or three-dimensional growth mode, is the opposite situation in which many crystal layers grow at the same time causing the surface to form hillocks and cavities. Between the Frank–van der Merwe and the Volmer–Weber growth modes, the intermediate case is the Stranski–Krastanov growth mode, where the deposit first grows layer by layer on the substrate and then, beyond a few layers, the growth becomes three dimensional.[57] These cases have a microscopic origin and are dependent on the interatomic forces of the actual deposit/surface material.[56]

From a theoretical perspective, the ability to fully simulate the entire MAPI crystallization process remains an unresolved challenge. First principles atomistic simulations have made a substantial contribution to the study of growth-related properties, including the formation reaction,[58] cohesion,[59] defect thermodynamics[60] and degradation pathways.[61] Nevertheless, all these approaches, due to their high computational cost, cannot simulate crystallization phenomena at finite temperature.

On the other hand, classical molecular dynamics models (*e.g.*, MYP model[62]) are capable of dealing with many thermodynamical properties of 2D,[63,64] 3D,[65,66] and complex-phase systems.[67–69] So far, the widely used MYP0[62] and MYP1[33] force fields have not yet been able to simulate the reaction of precursors (the salt halides, PbI_2 and MAI) into the MAPI crystal, even in dry conditions. To date, the only studies of crystallization focused on inorganic perovskites[70] or on different hybrid perovskites, *i.e.*, $FAPbI_3$.[71] In the latter case, a polarizable model was used, but its high computational cost prevented a comprehensive analysis, including the growth velocity versus temperature.

We have very recently proved that it is possible to enhance the aforementioned MYP0 ionic models by developing an efficient many-body force field (*i.e.* the MYP2) that can rectify the representation of clusters and facilitate the direct simulation of crystal formation.[72] The MYP2 model contains many-body (*e.g.* angular) terms that are chosen to reproduce the structures of Pb_nI_m and hybrid clusters MA_4PbI_6 and the mechanism and energy barrier of the formation of the crystalline bulk from precursors.[72] Alternative models containing angular terms, such as the ReaxFF,[73,74] could be in principle able to simulate crystallization but we are not aware of available force-fields for $MAPbI_3$. On the other hand, machine learning force-fields (MLFF) offers a flexible and potentially more accurate alternative[75,76] but the training for complex microstructures and growth still remain challenging. Furthermore, standard MLFF models do not incorporate atomic charges and electrostatics that are crucial for ionic diffusion and growth. The merit of MYP2 is attributable to its simplicity and to the physical interpretation of its terms, which facilitates the selection of parameters.

Here, by applying this MYP2 force-field to large atomistic models in the microsecond time scale, we have made significant strides in visualizing, characterizing, and understanding at the atomistic scale the process of spontaneous MAPI crystal formation from premixed precursors. In detail, we have identified the mechanisms and the activation energy of the crystal growth, as well as the diffusivity of ionic species throughout this growth phase. Furthermore, we have characterized the morphology of the crystalline front as a Stranski-Krastanov type growth, and the types of defects that spontaneously form during growth.

Results

Deposition and Disorder of Precursors on the (001) Crystalline MAPI surface

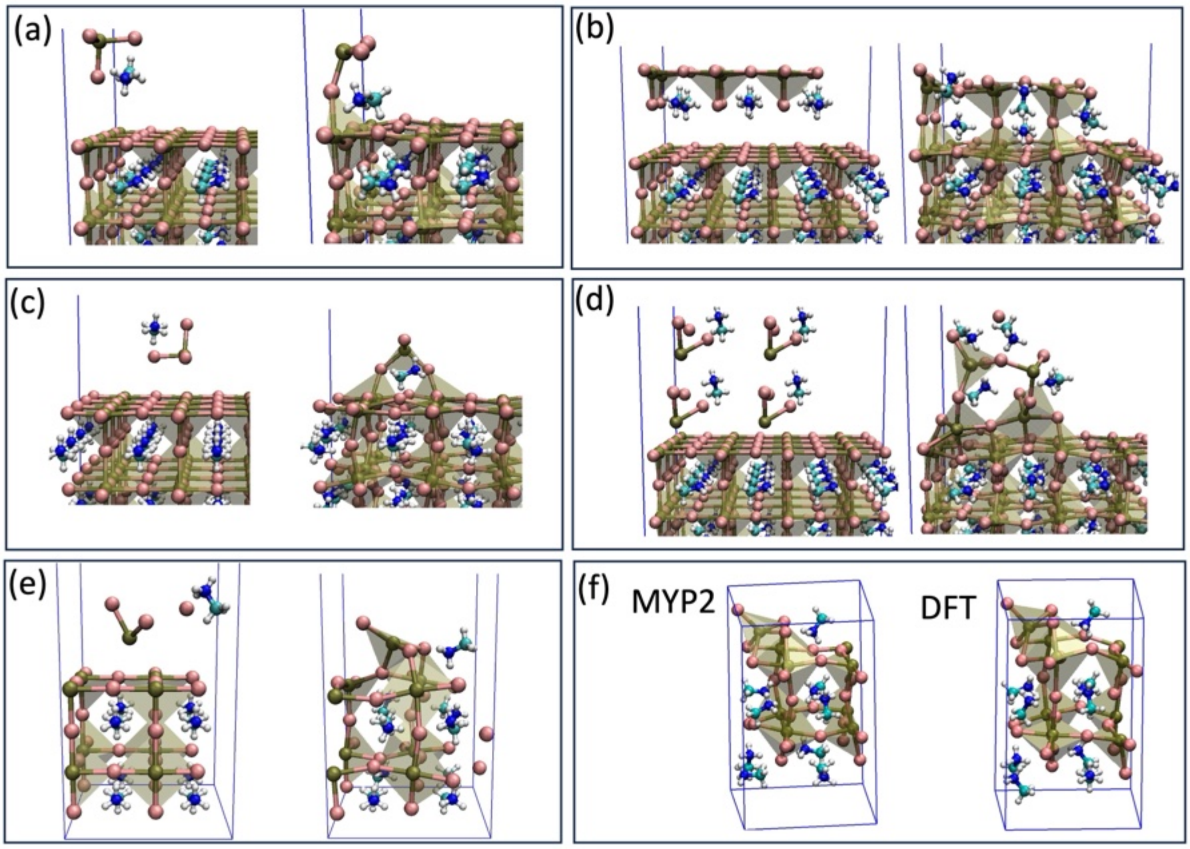

Figure 1: Mechanisms of adhesion of deposited precursors on the Pb-terminated (001) crystalline surface; (panel a) one $MAPbI_3$ unit with favorable orientation; (panel b) four units with same orientation; (panel c) non-crstalline configuration from rotated $MAPbI_3$ unit; (panel d) disordered configuration from four co-deposited PbI_2 and four MAI units; (panel e) non-crystalline configuration from co-deposited PbI_2 and MAI ; (panel f) comparison of the atomistic structure of disordered configuration optimized by MYP2 (left) and by DFT (right).

To understand the mechanisms underlying crystal growth, we perform molecular dynamics (MD) simulations using the recently developed MYP2 model.[72] The surface properties (*e.g.* the interfacial dipoles[77] or the stability[78]) strongly depend on its orientations and terminations, likely affecting the growth kinetics and morphology. However, in this work we focus only on the relevant (001) crystalline surface of $MAPbI_3$. MD simulation of crystal growth along alternative crystallographic orientations will be subject of future investigations. We begin by examining the behavior of a single $MAPbI_3$ unit deposited onto a (001) crystalline surface at $T = 0$ K. Technical details and input files to perform all MD simulations discussed below are reported in the SI. When the $MAPbI_3$ unit is arranged in its most favorable orientation (Fig.1, panel a, left), MD simulations reveal that it bonds seamlessly to the surface, forming a crystalline edge (Fig.1, panel a, right). In this ideal configuration, the Pb atom and one of the deposited I atoms establish a vertical Pb–I–Pb edge characteristic of the perovskite cubic unit, with the MA molecule residing at the center of the forming cube. This suggests that under optimal conditions, the deposition of single units can directly contribute to crystalline growth. Extending this mechanism, we consider the arrangement of multiple units. When several $MAPbI_3$ units (*e.g.*, four units) are deposited in alignment (Fig.1, panel b, left), they collectively form a portion of a crystalline monolayer upon bonding to the surface (Fig.1, panel b, right). This indicates that ordered crystal growth is achievable when multiple units are added in favorable orientations.

However, in practical scenarios, deposited precursor units often have random orientations and distortions. For example, if a single $MAPbI_3$ unit is rotated upside down before deposition (Fig.1, panel c, left), the resulting configuration after bonding to the surface is non-crystalline (Fig.1, panel c, right). The Pb–I–Pb segment formed is not vertical, and the Pb atom does not align with the underlying Pb atoms of the surface. Correcting this misalignment to form a crystalline structure would require breaking existing Pb–I bonds and overcoming associated energy barriers (see results below). The disorder becomes more pronounced when we consider the deposition of multiple units with varying orientations. When two distinct precursor units—PbI_2 and MAI—are deposited in close proximity with random orientations (Fig. 1, panel e, left), their interactions lead to non-crystalline configurations. The deposited Pb may bind directly to a surface iodine, resulting in a structure where the Pb, MA molecule, and iodides are at the same altitude, lacking the layered arrangement of the crystal lattice. As the number of deposited units increases further (Fig.1, panel d, left), the variety of possible disordered configurations grows exponentially. The entropy associated with these configurations favors the formation of a disordered film.

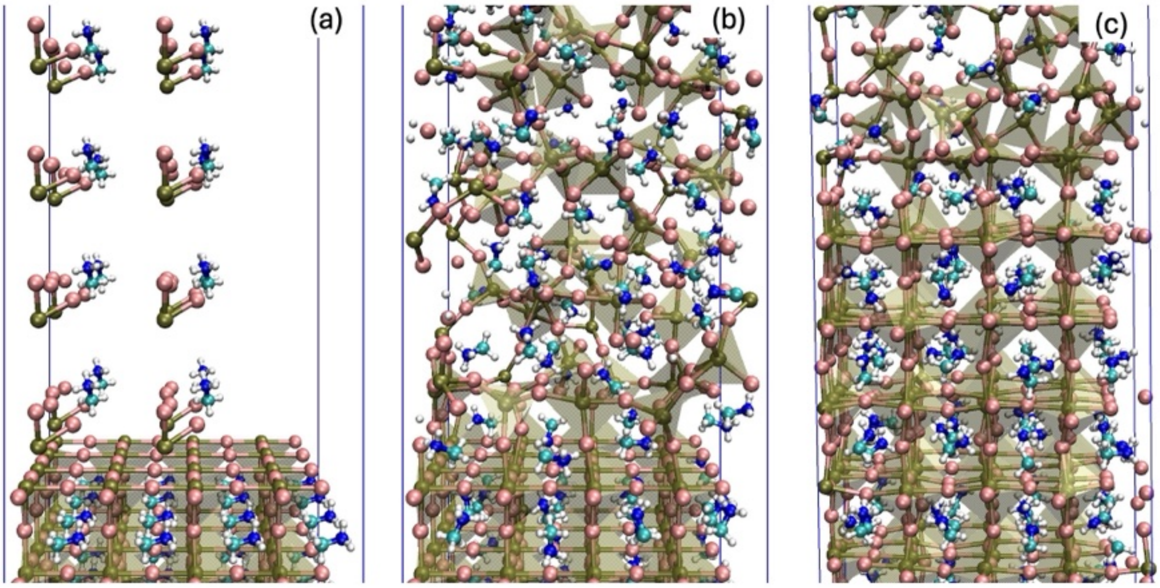

Figure 2: (a) Deposition of PbI_2 and MAI precursors on the (001) Pb-terminated $MAPbI_3$ crystalline surface; (b) Disordered film formed by the deposited precursors; (c) Crystallized $MAPbI_3$ film after annealing.

This is evident at finite temperatures MD simulations, where the initial deposition of multiple precursor units (Fig.2, panel a) results in a non-crystalline, low-density film that rapidly loses any initial order (Fig.2, panel b). Although atomistic simulations cannot precisely replicate real growth experiments we consider our initial conditions to represent a stoichiometric co-deposition of PbI_2 and MAI under conditions of high flux and low energy. The stoichiometric conditions of growth (*e.g.* the proportion of Pb atoms and Pb ions) constitutes a critical factor influencing the performance[79,80] and stability of perovskites (*e.g.* affected by Pb precipitation).[80,81] However, in this work we only consider stoichiometric conditions and leave other cases to future investigations.

From an experimental perspective, the disordered morphology of the deposit material obtained from MD can be described as amorphous PbI_2, intercalated with MAI salt. Over time, this disordered layer compacts on the surface eventually initiating crystallization.

The transformation of this disordered layer into a well-ordered $MAPbI_3$ crystal does not occur instantaneosly; rather it necessitates prolonged simulation durations and thermal fluctation to promote crystallization, a phenomenon that is achievable with the current MYP2 model (refer to Fig.2, panel c), and whose intricacies will be elaborated upon in the subsequent discussion.

To validate our findings on disordered deposit material, we performed density functional theory (DFT) calculations (see Methods section for computational details). The existence of local minima corresponding to disordered structures predicted by MD simulations is confirmed by DFT results. An example is shown in Fig. 1, panel f, demonstrating qualitative structural agreement between the MYP2 and DFT optimization.

Kinetics of crystallization

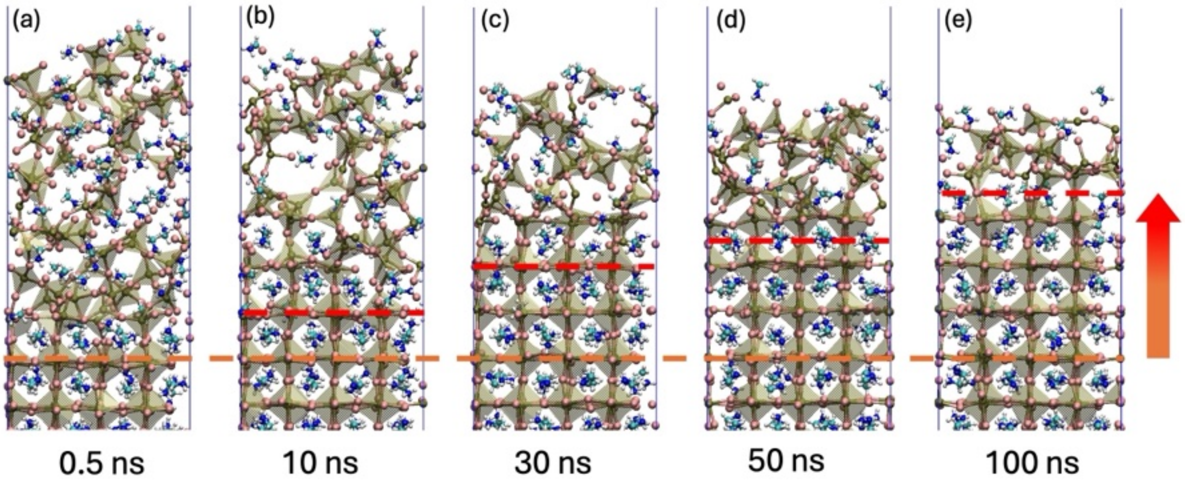

Figure 3: Snapshots derived from NPT trajectory elucidating the crystallization of the deposited precursors along the (001) MAPI crystallographic orientation.

The ability to simulate the crystallisation process from the disordered deposited film represents the central result of this study. This is made possible by the MYP2 interatomic model, which improves accuracy over existing techniques enabling MD simulations in the microsecond time scales (see Fig.3, panels a-e). These demonstrate that the crystallisation process is thermally activated, commencing from the substrate surface with a progressive advancement upwards (see Fig.3, red arrow), thereby realizing a mechanism of solid-phase epitaxial growth.[82–84]

For each temperature under consideration, it is possible to estimate the crystallization velocity through the calculation of the structure factor $S_{\vec{k}}(t)$ (see S.I). The obtained velocities as a function of temperature are reported in Fig. S5 as symbols; the green line represents the fitting kinetic model of Eq. 1.

$$v(T) = v_0 e^{-\frac{E_a}{kT}} \left(1 - e^{-\frac{\Delta H(T)}{kT}}\right) \tag{1}$$

The first factor of Eq. 1 contains the Arrhenius dependence $e^{-E_a/kT}$, with the activation energy E_a controlling the monotonic ascent of the curve. (Eq. 1 is further discussed in the SI.) The second multiplicative factor takes into account the energy difference, $\Delta H(T) \geq 0$, between the disordered and the crystalline phase; when $\Delta H = 0$ the crystallization is inhibited, *i.e.* $v = 0$. We model $\Delta H(T)$ as $|\Delta H_0|(1 - \frac{T}{T_0})^m$ and we fit all parameters to reproduce atomistic data. We find an activation energy of $E_a = 0.37$ eV, that controls the slope of the model in logarithmic scale (see Fig. 4, and Fig S3 for further details).

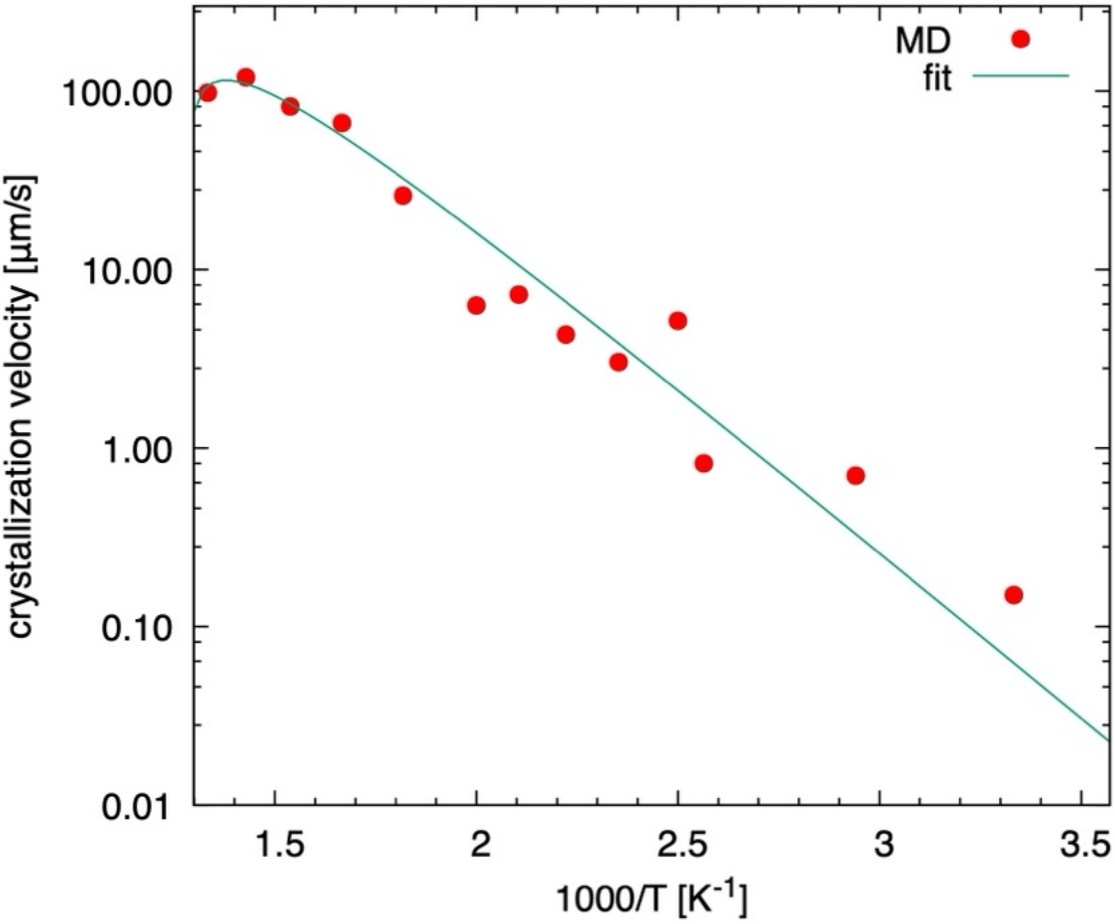

Figure 4: Crystallization velocities (red symbols) calculated by MD simulations as a function of temperature. The activation energy extracted from the fitting model (green line) corresponds to $E_a = 0.37$ eV.

This value represents the energy barrier of the microscopic processes controlling crystallisation. To our knowledge there are no experimental estimates of the activation energy in vacuum. For growth in solution (that involves radically different chemi-physical mechanisms with intermediate phases) data span a wide 0.15-1.0 eV interval,[85] depending on the solvents and the intermediate phases. Furthermore, considering that crystallization involves ions diffusion, we can compare with the activation energies for ionic migration in MAPI, for which experimental data are scattered within the range 0.1-1.0 eV[86] or above 0.26 eV when considering the cations.[87]

Microscopic origin of the activation energy

In order to achieve insight into the calculated activation energy, we select relevant atomistic sequences during annealing (Fig. 5, panels a-e). The process of crystallisation necessitates the rupture of Pb-I bonds, thereby facilitating the displacement of the lead and the opening of the structure with the formation of the cubic cage (Fig. 5, panel e). This process occurs at the crystal-disorder interface and involves a cooperative dynamics of

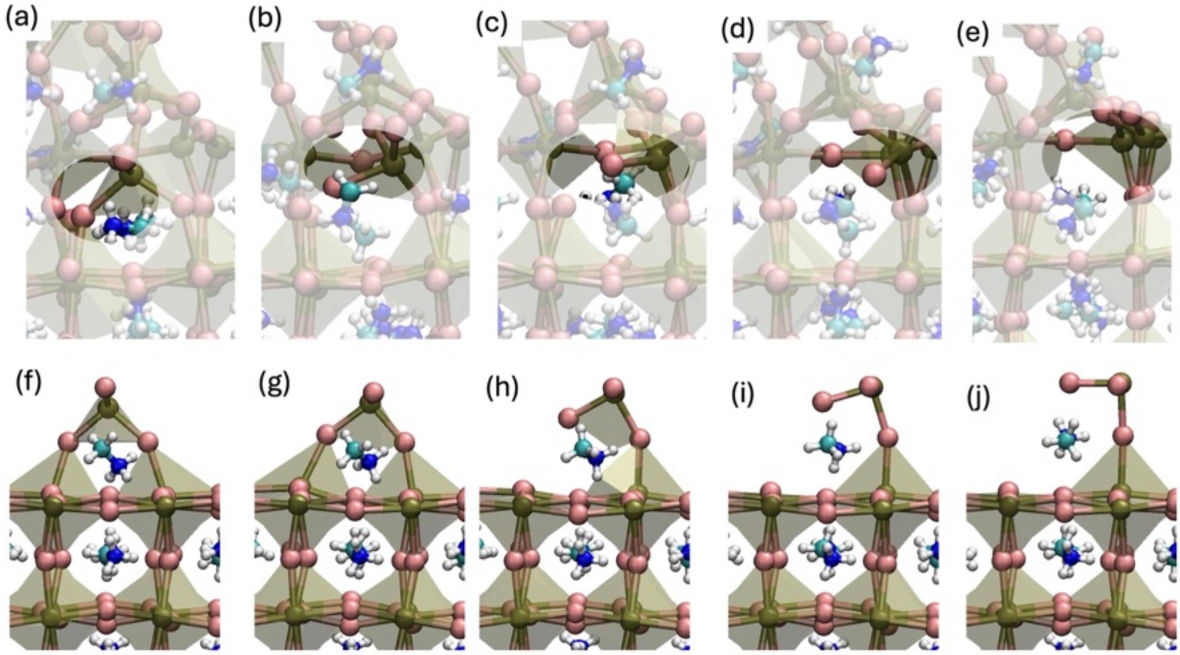

Figure 5: (panels a-e) microscopic mechanism of crystallization extracted from the NPT-MD trajectory at the order-disorder boundary; (panel f-j) similar mechanism simulated on the clean surface at 10 K.

surrounding atoms. The calculation of the associated energy barrier is difficult due to large fluctuations induced by temperature and by the large number of atoms. In order to facilitate the analysis, we consider the process described in Fig. 5, panels f-h. The initial configuration on the surface (panel f) mimics the same defective I-Pb-I dumbbell found at the interface (panel a) but on the perfect surface. During a low temperature (10 K) dynamic, a moment of increasing force is applied to the deposited precursor (panel f) until one Pb-I bond breaks and a cubic edge is formed (panel j). This allows us to estimate the energy barrier that is 0.45 eV. Considering that temperature effects reduces the static barrier (through vibrational and configurational entropy) we conclude that this value is compatible with the activation energy obtained from kinetics (0.37 eV). Further characterization, including that based on edge- and corner-sharing octahedra,[44] as well as radial and angular distribution[43] , will be the subject of future research. The analysis discussed above is already sufficient to conclude that the microscopic mechanisms of Pb-I bond breaking, as illustrated in Fig. 5, control the rate of crystallisation.

Ionic Diffusion during Crystallization

The process of crystal growth necessitates the vertical alternation of PbI and MAI planes; consequently, the mobility of deposited cations on the surface is of significant consequence to realize the crystalline order. While the mobility of ionic species in the crystal has been extensively investigated in literature,[61,88] this is not the case for the disordered PbI_2:MAI comprising precursors in contact with the crystalline surface.

Our atomistic trajectories permit us to estimate of the diffusivity of diverse species during growth at different temperatures (see Fig.6, panel a). Details on diffusivity calculations can be found in the SI. An in-plane (perspective) view of one atomistic crystallizing configuration is reported in the bottom panel of Fig.6, panel b , where MAs, iodine, and lead cations are represented in blue, red and green, respectively. A perspective view is reported in Fig.6, panel c. The large circles in panel b represent the areas in the xy plane (parallel to surface) explored by the corresponding cations during the dynamics (see S.I.). It is clear that, consistently with the calculated diffusivities, the displacements of MAs

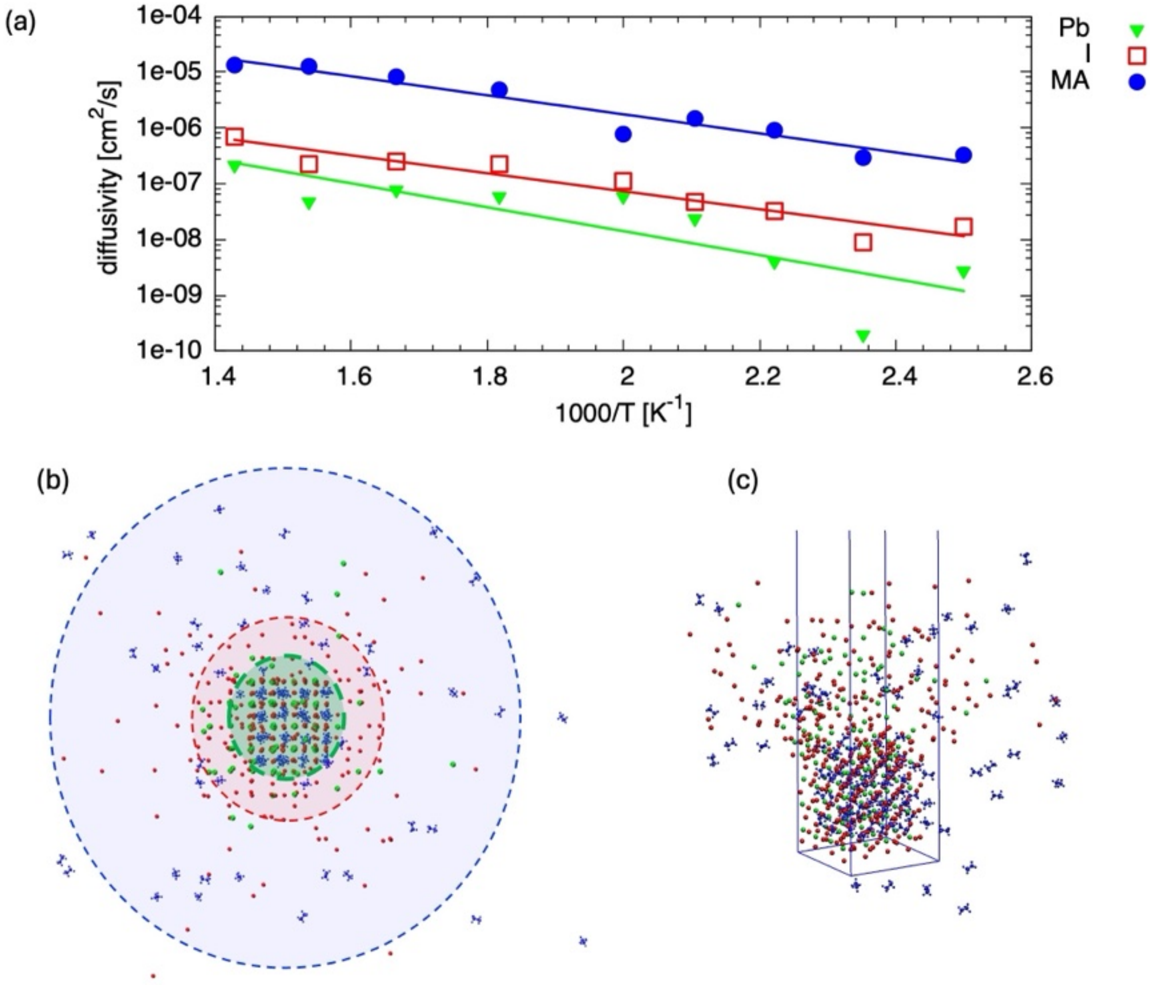

Figure 6: (panel a) diffusivity of Pb (green), I(red) and MA(blue) as a function of temperature, calculated during crystallization process; symbols are atomistic data and lines are Arrhenius fits; in-plane view (panel b) and perspective view (panel c) of an atomistic configuration showing the ions displacements (green, red and blue represent Pb, I and MA, respectively) after dynamics.

(blue area) and iodines (red area) are larger than lead (green area).

We can estimate the activation energies of MAs, iodines and lead to be 0.34 eV, 0.32 eV, and 0.42 eV, respectively. These results are intriguing for several reasons. First, the diffusivities in the present disordered phase are larger than in the crystalline one. Second, the molecules, not the iodines, are the most mobile ions during growth. A special role is played by the Pb metal cations which have the lowest mobility. The activation energy for Pb diffusion is 0.42 eV, which is close to the corresponding value for crystallisation. We conclude that diffusion of Pb (at the interface and in the disordered phase) activates the MAPI crystallization.

Morphology of the crystalline boundary

For technological applications, the quality and sharpness of MAPI interfaces are crucially important. For this, it is essential to not only comprehend the growth mechanisms but also to gain insight into the intrinsic morphology and its evolution during growth. To this end, supplementary simulations were conducted on larger systems.

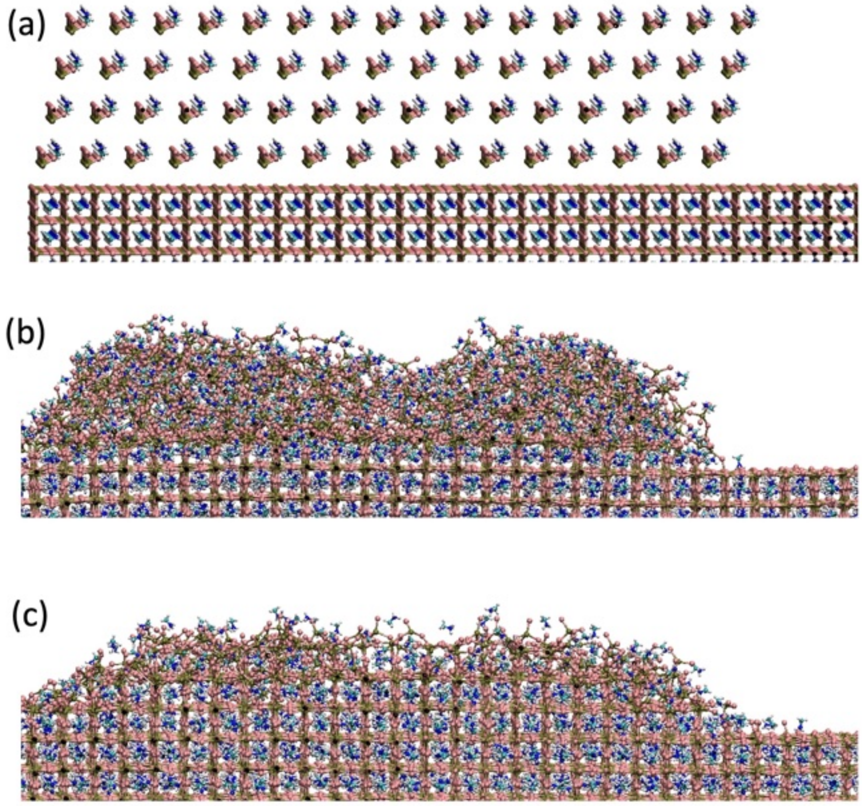

Figure 7: (Panel a) Cross-view of the 58416-atoms model consisting of 16 × 14 × 4 cluster of PbI_2 and MAI units deposited on a crystalline surface of area 19.5 nm × 19.4 nm; the fragments are initially distributed in a volume of 14 nm x 14 nm x 4 nm; (panel b) due to cohesive interatomic forces the fragments bind to the surface; (panel c) the disordered PbI_2:MAI cluster crystallizes according to a layer-by-layer bottom up process.

The first system is illustrated in Fig. 7 by which we study the crystallization of a large cluster of precursors on wide crystalline surface (from top to bottom panels). The system comprises a large surface (19.5 nm × 19.4 nm) on which 16 × 14 × 4 fragments (PbI_2 and MAI) have been deposited. The initial fragments are initially distributed periodically in a volume of 14 nm × 14 nm × 4 nm (Fig. 7, top panel). The size of the simulation box in the z direction is 12.1 nm that includes a large portion of empty space above the surface.

The computational effort is justified by the unprecedented insight into the microscopic in-plane crystal evolution. The in-plane views of the first PbI layer of the cluster during MD are reported in Fig. 8. In Fig.9 we additionally present the observations pertaining to the second layer (red) and the third layer (blue) after two microseconds dynamics at 700 K. From the analysis of trajectories we extract important information: (i) at high deposition dose, the precursors aggregate and adhere to the surface giving rise to a disordered nanocluster (Fig. 7, panel b,c); (ii) cohesive forces prevent the cluster spreading on the surface and maintain at least three atomic layers thickness (Fig. 7, panel c); (iii) in the plane of the surface (Fig. 8, panel a) the cluster is disordered but the boundaries are aligned on average along ⟨010⟩ and ⟨100⟩ crystallographic directions of the surface; (iv) the crystalline phase nucleates within the contact area (and not at the boundaries), giving rise to crystalline islands of the thickness of one atomic monolayer, oriented as the

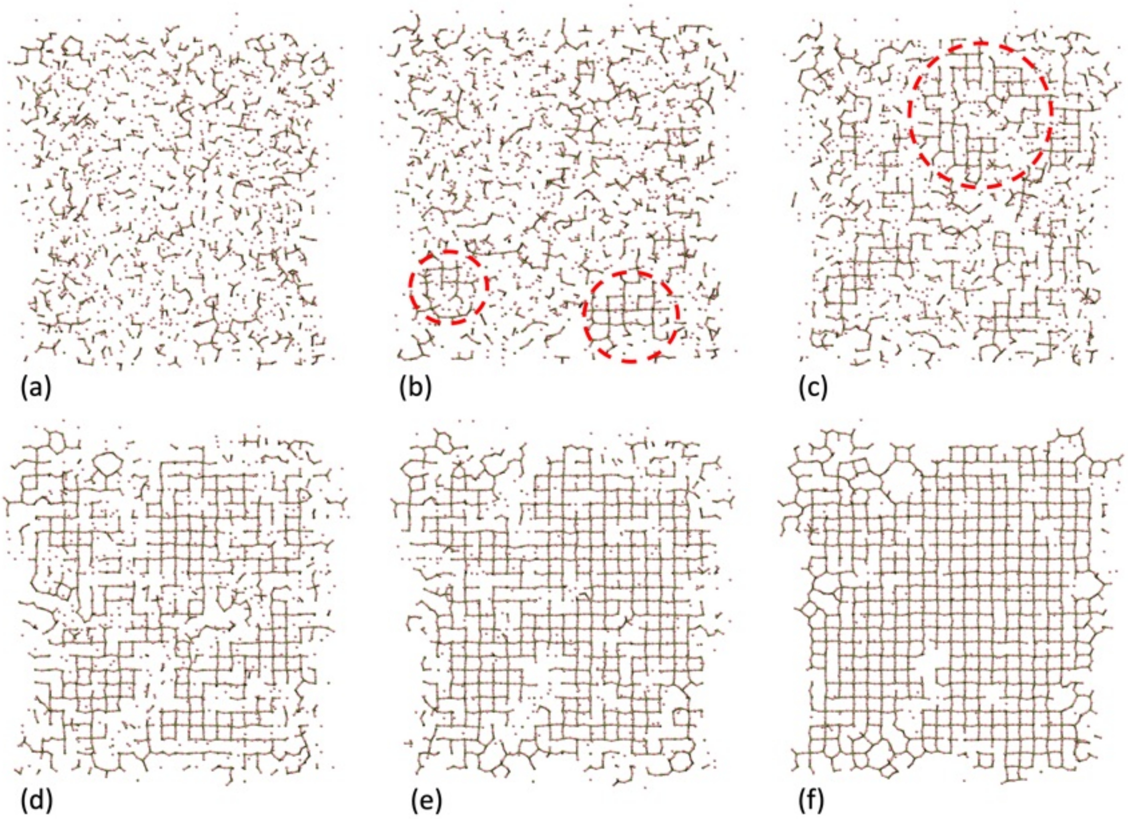

Figure 8: In-plane view of the first deposited layer on crystalline surface during crystallization from initial disordered configuration (panel a) to almost crystallized (panel f); red circles indicate crystalline nuclei;

underlying surface; (v) the crystalline islands grow rapidly in the plane, consuming the

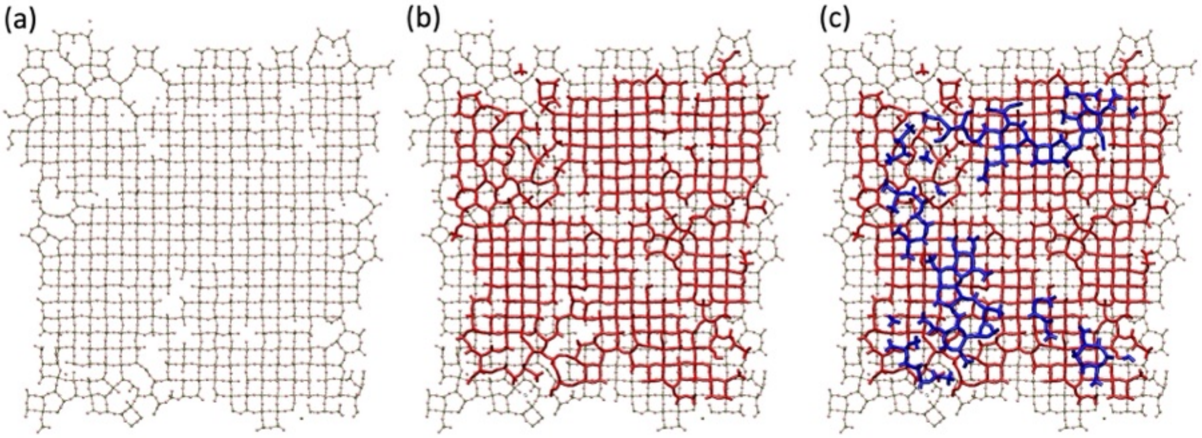

Figure 9: In-plane XY view of the first (panel a), the second (panel b) and third atomic layer (panel c) of the nanocrystal at the end of the simulation; the atoms of the second and third layers are highlighted in red and blue, respectively.

disorder phase along the ⟨100⟩ and ⟨011⟩ directions; (vi) the growth decelerates as the grains come into contact, resulting in the formation of a two-dimensional nanocrystalline structure with disordered boundaries. (vii) the subsequent evolution is slower leading to the crystallisation of the edges and the coalescence of the grains into a single crystalline domain, although with a residual structural disorder; (viii) the second layer (red atoms in Fig.9) commence crystallisation only subsequent to the underlying layer having locally ordered themselves; similarly the crystallization of the third layer (blue) occurs where the underlying atoms have already ordered (red). This step-by-step mechanism gives rise to a pyramidal crystalline front.

Overall, our results shows a growth process nucleating from the layer in contact with the surface and evolving layer-by-layer. At the end of the simulation the cluster has not been able to fully crystallize but exhibits some residual disorder particularly at the second and third layers.

To gain further insight into the cross-section morphology of the crystalline front, we additionally examine the systems illustrated in Fig. 10, where a 12 nm-thick layer of precursors has been deposited. Once more, the results are consistent with a layer-by-layer growth in the initial stages of crystallisation. The crystalline centres that nucleate at the interface extend into the plane of the interface while maintaining a planar surface

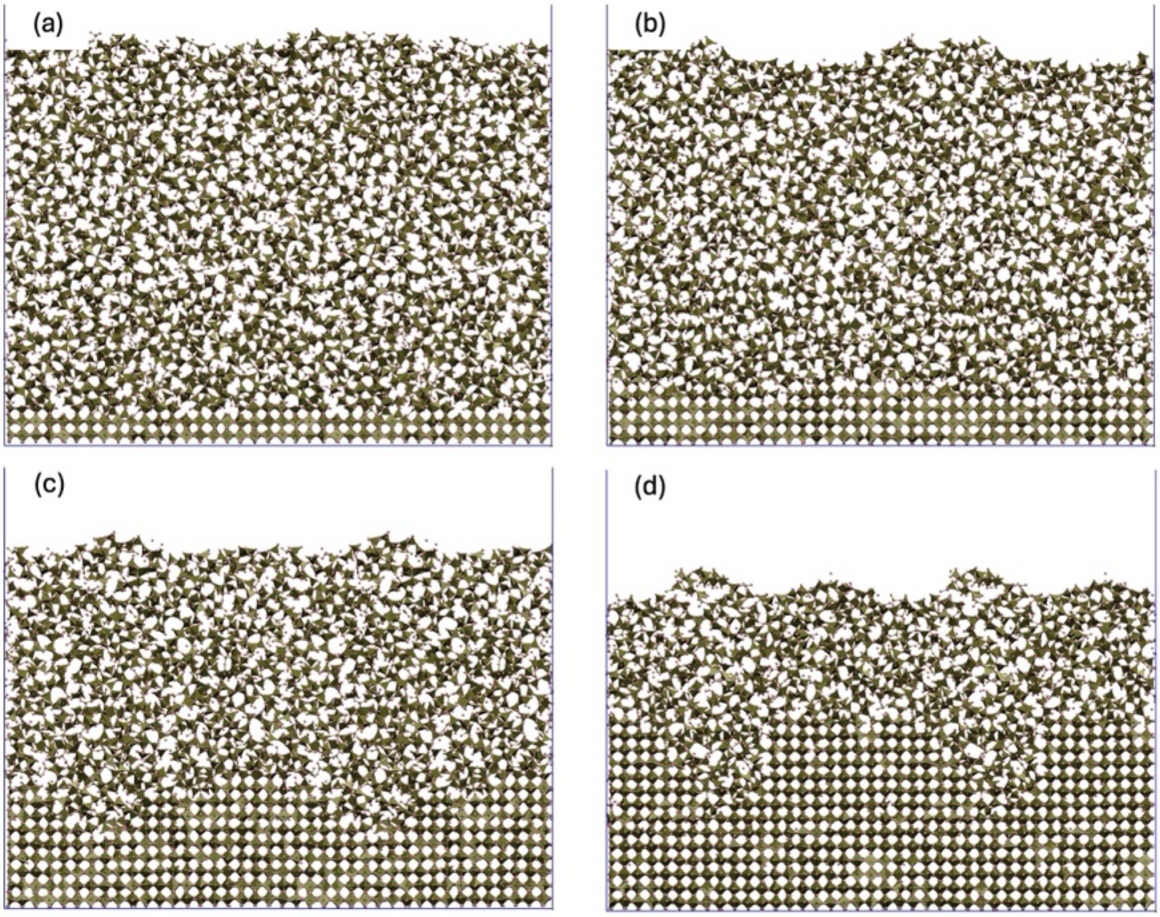

Figure 10: Cross-view of the atomistic system (consisting of a (001)-surface covered by 12 nm-thick film of precursors) during crystallization showing the evolution of the crystal morphology with time.

in the early stages (Fig.10, panels a,b). This shows that the in-plane growth velocity is greater than the out-of-plane velocity. At longer timescales and for larger surface areas, the nucleation of crystalline centres may occur even on partially crystallised upper layers. As a result, the initially planar structure of the interface undergoes a transformation, and the surface thickness increases. At longer times (∼20 ns), pyramidal structures emerge, enabling the attainment of roughness of 3-5 nm. The observed growth characteristics are located between the layer-by-layer and the three-dimensional growth models, and are consistent with the Stranski–Krastanov evolution (ee the section with this title in the Supporting Information).

Spontaneous formation of lead vacancies

We conclude our study with compelling findings on the formation of defects during the growth process. Point-defects are known to affect the optoelectronic properties and the stability of MAPI.[89] Iodine defects are abundant and mobile but they are shallow and optically inactive;[90] on the contrary, experiments and calculations identify lead vacancies, V_{Pb}, as stable and optically active centers in $MAPbI_3$. They give rise to hole trapping[91] with deep (0/2–) charge transition located 0.5 eV above the valence band.[92,93]

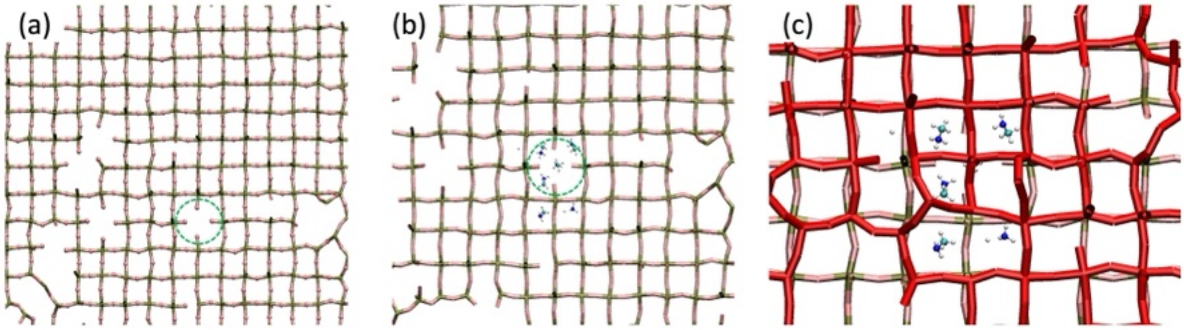

Figure 11: Lead vacancy formation during the crystallization process; (panel a) the lead vacancy (green circle) appears in the PbI monolayer; (panel b) the surrounding MA molecules diffuse around the defect and occasionally occupy the position of the missing lead atom; (panel c) the overlaying PbI layer (red) traps the vacancy into the grown crystal.

Most atomistic studies, investigate the formation of defects statically by introducing defects and by comparing the energetics to that of the perfect bulk.[94] Interestingly, our MD simulations make it possible to observe and explain the mechanism of formation of lead vacancy during crystallization at finite temperature. The crystallization proceeds by first forming a MAI plane that is then progressively covered by a subsequent PbI plane. The crystallization of the latter plane is slower and, due to the low diffusivity of Pb cations, contain several V_{Pb} lead vacancies (see Fig. 11, panel a, green circle) mainly located at the boundaries of the growing crystalline PbI nuclei. The vacancies are negative with charge opposite to that of the missing lead cation. At low crystallization rate, the vacancies are eventually saturated by lead atoms arriving from the neighboring regions of the precursors film. However, the positively charged MAs molecules can be captured by the negative V_{Pb} due to the attractive electrostatic interaction; the result is a longliving metastable V_{Pb}-MA[95] (see Fig. 11, panel b) complex that can be buried into the crystal if the overlaying MAI plane (Fig. 11, panel c, red) is rapidly formed. As we have concentrated on stoichiometric conditions, the presence of vacancies at the crystal-amorphous interface indicates the presence of excess lead atoms in the superior disordered layers. This occurs due to the slow diffusion of metal cations. Since the formation of vacancies at the interface, the restoration of a perfect crystal is unlikely to occur, because it is requested the reaction with an interstitial lead, but this is a rare event due to the low mobility of metal cations in the crystalline phase.[90] The result is a stable lead vancancy V_{Pb} in the crystallized film. At high growth rates we also observed the formation of cation-cation antisite, MA_{Pb}, obtained by an interstitial MA cation that occupies the lead vacancy. In line with our findings, by static DFT calculations, Xue et al.[96] found that in the inorganic $\mathrm{CsPbI_3}$ crystal, under nonequilibrium conditions, sizeable concentrations of lead vacancies $\mathrm{V}_{Pb}{}^{2-}$ and cation–cation antisites Cs_{Pb}^{-} are expected.

From this analysis, we conclude that the formation of lead vancancy is driven by the kinetics of growth rather than the equilibrium thermodynamics and the final concentration is related to the balance within crystallization velocity and mobility of ions. In other words, it is in principle possible to reduce the concentration of such defects at lower kinetics (controlling T and deposition flux) or with strategies to increasing the mobility of lead (*e.g.* with excess PbI).

Conclusions

In conclusion, by means of new model potential MYP2 we have studied the crystallization of $\mathrm{MAPI_3}$ during annealing; the temperature dependence of the growth velocity is described by an activation energy 0.37 eV, a value that we associate to the break up of defective Pb-I bonds and to the energy barriers for diffusion of lead cations at the disorder-crystal interface (0.4 eV). The crystal evolution with time exhibits the morphological features of the Straski-Krastanov growth with surface roughness increasing during the annealing, consistently with observations in evaporated material. Remarkably, we have observed and analysed the mechanisms of spontaneous formation of lead vacancies, suggesting a kinetic origin of such an optically active defects and the possibility, in principle, to reduce their concentration reducing annealing temperature and deposition rate or by strategies to enhance lead diffusivity.

Methods and Simulations

The MYP2 force-field is obtained by starting from the MYP0 and adding an extra many-body functional (MB) acting on inorganic atoms. The MYP0 model[62] encompasses the sum of organic-organic U_{OO}, inorganic-inorganic U_{II} and organic-inorganic U_{OI} terms. The U_{OO} has the functional form of the standard GAFF force field including bonds, angles, dihedrals, electrostatic and dispersive interactions.[97] The U_{II} inorganic Pb-I interactions are described by Buckingham-Coulomb potential.[98,99] As for U_{IO}, they are the sum of nonbonding Buckingham, Coulomb and Lennard-Jones 12-6 (LJ) terms.

The rationale of MYP2 is to model the covalent (*i.e.* directional) character of the Pb-I bonding (that is not otherwise included within the pure ionic MYP0 model) by adding Tersoff terms;[72] for a comprehensive description see Ref.[72] Molecular dynamics calculations were performed by the LAMMPS software.[100] The time step was chosen equal to 1 fs. We made use of the overlay functionality and the pair_style *hybrid overlay tersoff lj/charmm/coul/long 9.9 10.0 buck/coul/long 9.9 10.* When directly comparing DFT and MD clusters, we made use of identical simulation boxes. Instananeous crystalline fraction were calculated through the structure factor, $S_{\vec{k}}(t)$,

$$S_{\vec{k}}(t) = |\frac{1}{N} \sum_{r=1,N} e^{i\vec{k}\cdot\vec{x}_r(t)}| \tag{2}$$

which is the spatial Fourier transform of the atomic positions, x_r, of the N atoms of the system evaluated in the reciprocal space of the crystal with reciprocal vector $\vec{k}$; we chose (k=$\frac{2\pi}{L_0}$,0,0) with L_0 close to the Pb-I lattice spacing (see S.I.). The value of $S_{\vec{k}}$ approaches one in a perfect crystal or zero in a totally disordered system.

The ab-initio calculations were performed using the plane wave basis set code Quantum Espresso version 7.3[101,102] , applying Density Functional Theory (DFT) through the Perdew-Burke-Ernzerhof (PBE) exchange-correlation functional.[103] This is used in combination with projector augmented-wave (PAW) pseudopotentials from PseudoDojo[104] to describe the interaction between ions and electrons. The kinetic energy cutoff is set to 20 Ry. The convergence of the self-consistent field (SCF) calculation is considered achieved when the total energy changes by less than 10^{-6} Ry and the interatomic forces by less than 10^{-5} Ry/Å. Graphical representations of atomistic structures were made with VMD software[105] and GNUplot[106] crystallization and diffusivity plots. The input files to reproduce all the MYP2 and DFT calculations performed in this work are available in the SI.

Supporting Information Available

The supporting material includes the structures and control files for molecular dynamics simulations (file suppporting.tgz). The Supporting Information document (PDF) contains additional details related to: (i) crystallization evolution with time; (ii) kinetic model used to fit the crystallization data; (iii) calculation of the static energy barrier for crystallization; (iv) crystallization at different temperatures; (v) Stranki-Krastanov mechanisms of crystal growth.

Acknowledgements

AM, SA and CT acknowledges ICSC - CentroNazionale diRicerca in High Performance Computing, Big Data and Quantum Computing, funded by European Union -Next Generation EU - PNRR, Missione 4 Componente 2 Investimento 1.4 (B93C22000620006), and Project MUR-PRIN 2022 NEWATOMISTS (B53D23004630006) and Project MUR - PRIN 2022 PNRR ORIENTING (B53D23025530001) funded by European Union - NextGenerationEU -PNRR, Missione 4 Componente 2 Investimento 1.1; CC acknowledges Project MUR-PRIN 2022 IMPACT (B53D23015220006) and HADES (B53D23028700001) funded by European Union - Next Generation EU - PNRR, Missione 4 Componente 2

Investimento 1.1; AF and DD acknowledge project NEST funded under the National Recovery and Resilience Plan (NRRP), Mission 4 Component 2 Investment 1.3 -Call for tender No.1561 of11.10.2022 of Ministero dell'Università edella Ricerca (MUR), funded by the European Union NextGeneration EU; AF acknowledges project PRIN 2022 "TOTEM" (F53D23001080006) and project PNRR-PRIN 2022 "MAGIC" (F53D23008340001) funded by Ministero dell'Universita e della Ricerca (MUR). All Authors acknowledge CINECA for computational support through the ISCRA initiative.

References

1. Weber, D. CH3NH3PbX3, ein Pb(II)-System mit kubischer Perowskitstruktur / CH3NH3PbX3, a Pb(II)-System with Cubic Perovskite Structure. *Zeitschrift für Naturforschung B* **1978**, *33*, 1443–1445, Publisher: De Gruyter.

2. Møller, C. K. Crystal Structure and Photoconductivity of Cæsium Plumbohalides. *Nature* **1958**, *182*, 1436–1436, Publisher: Nature Publishing Group.

3. Mattoni, A.; Filippetti, A.; Caddeo, C. *Structure and Thermodynamic Properties of Hybrid Perovskites by Classical Molecular Dynamics*; 2017; pp 1–42.

4. Poglitsch, A.; Weber, D. Dynamic disorder in methylammoniumtrihalogenoplumbates (II) observed by millimeter-wave spectroscopy. *The Journal of Chemical Physics* **1987**, *87*, 6373–6378.

5. Li, H.; Lin, H.; Ouyang, D.; Yao, C.; Li, C.; Sun, J.; Song, Y.; Wang, Y.; Yan, Y.; Wang, Y.; Dong, Q.; Choy, W. C. H. Efficient and Stable Red Perovskite Light-Emitting Diodes with Operational Stability >300 h. *Advanced Materials* **2021**, *33*.

6. Zhang, J. Enhanced Phase Stability and Reduced Bandgap for CsPbI3 Perovskite through Bi3+ and Cl– Co-Doping. *Russian Journal of Physical Chemistry A* **2024**, *98*, 2146–2151.

7. Li, Z.; Yang, M.; Park, J.-S.; Wei, S.-H.; Berry, J. J.; Zhu, K. Stabilizing Perovskite

Structures by Tuning Tolerance Factor: Formation of Formamidinium and Cesium Lead Iodide Solid-State Alloys. *Chem. Mater.* **2016**, *28*, 284–292, Publisher: American Chemical Society.

8. Mitzi, D. B. *Progress in Inorganic Chemistry*; John Wiley & Sons, Ltd, 1999; pp 1–121, _eprint: https://onlinelibrary.wiley.com/doi/pdf/10.1002/9780470166499.ch1.

9. Kojima, A.; Teshima, K.; Shirai, Y.; Miyasaka, T. Organometal Halide Perovskites as Visible-Light Sensitizers for Photovoltaic Cells. *J. Am. Chem. Soc.* **2009**, *131*, 6050–6051, Publisher: American Chemical Society.

10. Zhang, H.; Zhang, S.; Ji, X.; He, J.; Guo, H.; Wang, S.; Wu, W.; Zhu, W.; Wu, Y. Formamidinium Lead Iodide-Based Inverted Perovskite Solar Cells with Efficiency over 25

11. Hu, J.; Yang, L.; Zhang, J. A Review on Strategies to Fabricate and Stabilize Phase-Pure α-FAPbI3 Perovskite Solar Cells. *Solar RRL* **2023**, *7*.

12. Tsai, C. L.; Chang, S. H.; Jeng, M.-J.; Chang, L.-B.; Sharma, M.; Yuan, C.-T. Properties of FAPbI3-Based Alloy Perovskite Thin Films and Their Application in Solar Cells. *Processes* **2023**, *11*, 1450–1450.

13. Green, M. A.; Dunlop, E. D.; Yoshita, M.; Kopidakis, N.; Bothe, K.; Siefer, G.; Hinken, D.; Rauer, M.; Hohl-Ebinger, J.; Hao, X. Solar cell efficiency tables (Version 64). *Progress in Photovoltaics* **2024**, *32*, 425–441.

14. Best Research-Cell Efficiency Chart. `https://www.nrel.gov/pv/cell-efficiency.html`, accessed September 30, 2024.

15. Chin, X. Y.; Turkay, D.; Steele, J. A.; Tabean, S.; Eswara, S.; Mensi, M.; Fiala, P.; Wolff, C. M.; Paracchino, A.; Artuk, K.; Jacobs, D.; Guesnay, Q.; Sahli, F.; Andreatta, G.; Boccard, M.; Jeangros, Q.; Ballif, C. Interface passivation for 31.25%-efficient perovskite/silicon tandem solar cells. *Science* **2023**, *381*, 59–63, Publisher: American Association for the Advancement of Science.

16. Yin, W.-J.; Shi, T.; Yan, Y. Unique Properties of Halide Perovskites as Possible Origins of the Superior Solar Cell Performance. *Advanced Materials* **2014**, *26*, 4653–4658, _eprint: https://onlinelibrary.wiley.com/doi/pdf/10.1002/adma.201306281.

17. Fortino, M.; Mattoni, A.; Pietropaolo, A. Atomistic modeling of metal–ligand chirality transfer and chiroptical properties of lead and tin hybrid perovskites. *J. Mater. Chem. C* **2023**, *11*, 9135–9143, Publisher: The Royal Society of Chemistry.

18. Filippetti, A.; Wadhwa, P.; Caddeo, C.; Mattoni, A. A promising outlook on the development of lead halide perovskites as spin-orbitronic materials. *Applied Physics Letters* **2022**, *121*, 200501.

19. Filippetti, A.; Wadhwa, P.; Caddeo, C.; Mattoni, A. Fermi Surface Topology and Rashba-Edelstein Charge-Spin Conversion in Lead-Halide Perovskites. *Advanced Theory and Simulations* **2023**, *6*, 2300092.

20. Pietropaolo, A.; Mattoni, A.; Pica, G.; Fortino, M.; Schifino, G.; Grancini, G. Rationalizing the design and implementation of chiral hybrid perovskites. *Chem* **2022**, *8*, 1231–1253.

21. Filippetti, A.; Caddeo, C.; Delugas, P.; Mattoni, A. Appealing Perspectives of Hybrid Lead–Iodide Perovskites as Thermoelectric Materials. *J. Phys. Chem. C* **2016**, *120*, 28472–28479, Publisher: American Chemical Society.

22. Tantardini, C.; Kokott, S.; Gonze, X.; Levchenko, S. V.; Saidi, W. A. “Self-trapping” in solar cell hybrid inorganic-organic perovskite absorbers. *Applied Materials Today* **2022**, *26*, 101380.

23. Wehrenfennig, C.; Liu, M.; Snaith, H. J.; Johnston, M. B.; Herz, L. M. Homogeneous Emission Line Broadening in the Organo Lead Halide Perovskite CH3NH3PbI3–xClx. *J. Phys. Chem. Lett.* **2014**, *5*, 1300–1306, Publisher: American Chemical Society.

24. Herz, L. M. Charge-Carrier Mobilities in Metal Halide Perovskites: Fundamental Mechanisms and Limits. *ACS Energy Lett.* **2017**, *2*, 1539–1548, Publisher: American Chemical Society.

25. Chiarella, F.; Zappettini, A.; Licci, F.; Borriello, I.; Cantele, G.; Ninno, D.; Cassinese, A.; Vaglio, R. Combined experimental and theoretical investigation of optical, structural, and electronic properties of CH3NH3SnX3 thin films X=Cl,Br. *Phys. Rev. B* **2008**, *77*, 045129, Publisher: American Physical Society.

26. Dong, Q.; Fang, Y.; Shao, Y.; Mulligan, P.; Qiu, J.; Cao, L.; Huang, J. Electron-hole diffusion lengths $>$ 175 μm in solution-grown CH3NH3PbI3 single crystals. *Science* **2015**, *347*, 967–970, Publisher: American Association for the Advancement of Science.

27. Filippetti, A.; Delugas, P.; Mattoni, A. Radiative Recombination and Photoconversion of Methylammonium Lead Iodide Perovskite by First Principles: Properties of an Inorganic Semiconductor within a Hybrid Body. *J. Phys. Chem. C* **2014**, *118*, 24843–24853, Publisher: American Chemical Society.

28. Stranks, S. D.; Eperon, G. E.; Grancini, G.; Menelaou, C.; Alcocer, M. J. P.; Leijtens, T.; Herz, L. M.; Petrozza, A.; Snaith, H. J. Electron-Hole Diffusion Lengths Exceeding 1 Micrometer in an Organometal Trihalide Perovskite Absorber. *Science* **2013**, *342*, 341–344, Publisher: American Association for the Advancement of Science.

29. Kim, G.-W.; Petrozza, A. Defect Tolerance and Intolerance in Metal-Halide Perovskites. *Advanced Energy Materials* **2020**, *10*, 2001959, _eprint: https://onlinelibrary.wiley.com/doi/pdf/10.1002/aenm.202001959.

30. Conings, B.; Drijkoningen, J.; Gauquelin, N.; Babayigit, A.; D'Haen, J.; D'Olieslaeger, L.; Ethirajan, A.; Verbeeck, J.; Manca, J.; Mosconi, E.; Angelis, F. D.; Boyen, H.-G. Intrinsic Thermal Instability of Methylammonium Lead

Trihalide Perovskite. *Advanced Energy Materials* **2015**, *5*, 1500477, _eprint: https://onlinelibrary.wiley.com/doi/pdf/10.1002/aenm.201500477.

31. Akbulatov, A. F.; Luchkin, S. Y.; Frolova, L. A.; Dremova, N. N.; Gerasimov, K. L.; Zhidkov, I. S.; Anokhin, D. V.; Kurmaev, E. Z.; Stevenson, K. J.; Troshin, P. A. Probing the Intrinsic Thermal and Photochemical Stability of Hybrid and Inorganic Lead Halide Perovskites. *J. Phys. Chem. Lett.* **2017**, *8*, 1211–1218, Publisher: American Chemical Society.

32. Caddeo, C.; Marongiu, D.; Meloni, S.; Filippetti, A.; Quochi, F.; Saba, M.; Mattoni, A. Hydrophilicity and Water Contact Angle on Methylammonium Lead Iodide. *Advanced Materials Interfaces* **2019**, *6*, 1801173, _eprint: https://onlinelibrary.wiley.com/doi/pdf/10.1002/admi.201801173.

33. Caddeo, C.; Saba, M. I.; Meloni, S.; Filippetti, A.; Mattoni, A. Collective Molecular Mechanisms in the CH3NH3PbI3 Dissolution by Liquid Water. *ACS Nano* **2017**, *11*, 9183–9190, Publisher: American Chemical Society.

34. Ogomi, Y.; Morita, A.; Tsukamoto, S.; Saitho, T.; Fujikawa, N.; Shen, Q.; Toyoda, T.; Yoshino, K.; Pandey, S. S.; Ma, T.; Hayase, S. CH3NH3SnxPb(1–x)I3 Perovskite Solar Cells Covering up to 1060 nm. *J. Phys. Chem. Lett.* **2014**, *5*, 1004–1011, Publisher: American Chemical Society.

35. Abate, A. Perovskite Solar Cells Go Lead Free. *Joule* **2017**, *1*, 659–664, Publisher: Elsevier.

36. Ke, W.; Kanatzidis, M. G. Prospects for low-toxicity lead-free perovskite solar cells. *Nat Commun* **2019**, *10*, 965, Publisher: Nature Publishing Group.

37. Saidaminov, M. I.; Abdelhady, A. L.; Murali, B.; Alarousu, E.; Burlakov, V. M.; Peng, W.; Dursun, I.; Wang, L.; He, Y.; Maculan, G.; Goriely, A.; Wu, T.; Mohammed, O. F.; Bakr, O. M. High-quality bulk hybrid perovskite single crystals within minutes by inverse temperature crystallization. *Nat Commun* **2015**, *6*, 7586, Publisher: Nature Publishing Group.

38. Liu, D.; Zheng, Y.; Sui, X. Y.; Wu, X. F.; Zou, C.; Peng, Y.; Liu, X.; Lin, M.; Wei, Z.; Zhou, H.; Yao, Y.-F.; Dai, S.; Yuan, H.; Yang, H. G.; Yang, S.; Hou, Y. Universal growth of perovskite thin monocrystals from high solute flux for sensitive self-driven X-ray detection. *Nat Commun* **2024**, *15*, 2390, Publisher: Nature Publishing Group.

39. Min, H.; Wang, N.; Chen, N.; Tong, Y.; Wang, Y.; Wang, J.; Liu, J.; Wang, S.; Wu, X.; Yang, P.; Shi, H.; Zhuo, C.; Chen, Q.; Li, J.; Zhang, D.; Lu, X.; Zhu, C.; Peng, Q.; Zhu, L.; Chang, J. *et al.* Spin coating epitaxial heterodimensional tin perovskites for light-emitting diodes. *Nat. Nanotechnol.* **2024**, *19*, 632–637, Publisher: Nature Publishing Group.

40. Matsumoto, S.; Kumazawa, K.; Ogura, K. Novel Solvent-Free Reactions with Iodine: Solid–Solid and Solid–Vapor Reactions of 1-Aryl-4-(methylthio)-2-(p-tolylsulfonyl)-1,3-butadienes. *Bulletin of the Chemical Society of Japan* **2003**, *76*, 2179–2182.

41. Salah, M. B. H.; Mercier, N.; Dabos-Seignon, S.; Botta, C. Solvent-Free Preparation and Moderate Congruent Melting Temperature of Layered Lead Iodide Perovskites for Thin-Film Formation. *Angewandte Chemie International Edition* **2022**, *61*, e202206665.

42. Lee, J.-W.; Lee, D.-K.; Jeong, D.-N.; Park, N.-G. Control of Crystal Growth toward Scalable Fabrication of Perovskite Solar Cells. *Advanced Functional Materials* **2019**, *29*, 1807047, _eprint: https://onlinelibrary.wiley.com/doi/pdf/10.1002/adfm.201807047.

43. Kaiser, W.; Mosconi, E.; Alothman, A. A.; Meggiolaro, D.; Gagliardi, A.; De Angelis, F. Halide-driven formation of lead halide perovskites: insight from ab initio molecular dynamics simulations. *Materials Advances* **2021**, *2*, 3915–3926.

44. Ahlawat, P.; Dar, M. I.; Piaggi, P.; Grätzel, M.; Parrinello, M.; Rothlisberger, U. Atomistic Mechanism of the Nucleation of Methylammonium Lead Iodide Perovskite from Solution. *Chemistry of Materials* **2019**, *32*, 529–536.

45. Liu, C.; Cheng, Y.-B.; Ge, Z. Understanding of perovskite crystal growth and film formation in scalable deposition processes. *Chemical Society Reviews* **2020**, *49*, 1653–1687.

46. Wang, Z.; Lyu, M.; Zhang, B. W.; Xiao, M.; Zhang, C.; Han, E.; Wang, L. Thermally Evaporated Metal Halide Perovskites and Their Analogues: Film Fabrication, Applications and Beyond. *Small Methods* **2024**,

47. Lu, H.; Liu, Y.; Ahlawat, P.; Mishra, A.; Tress, W. R.; Eickemeyer, F. T.; Yang, Y.; Fu, F.; Wang, Z.; Avalos, C. E.; Carlsen, B. I.; Agarwalla, A.; Zhang, X.; Li, X.; Zhan, Y.; Zakeeruddin, S. M.; Emsley, L.; Rothlisberger, U.; Zheng, L.; Hagfeldt, A. *et al.* Vapor-assisted deposition of highly efficient, stable black-phase FAPbI 3 perovskite solar cells. *Science* **2020**, *370*.

48. Ng, A.; Ren, Z.; Shen, Q.; Cheung, S. H.; So, S. K.; Djurišić, A. B.; Wan, Y.; Wu, X.; Surya, C. Crystal Engineering for Low Defect Density and High Efficiency Hybrid Chemical Vapor Deposition Grown Perovskite Solar Cells. *ACS Appl. Mater. Interfaces* **2016**, *8*, 32805–32814, Publisher: American Chemical Society.

49. Xu, F.; Li, Y.; Yuan, B.; Zhang, Y.; Wei, H.; Wu, Y.; Cao, B. Large-area CsPbBr3 perovskite films grown with effective one-step RF-magnetron sputtering. *Journal of Applied Physics* **2021**, *129*, 245303.

50. Kosasih, F. U.; Erdenebileg, E.; Mathews, N.; Mhaisalkar, S. G.; Bruno, A. Thermal evaporation and hybrid deposition of perovskite solar cells and mini-modules. *Joule* **2022**, *6*, 2692–2734.

51. Sadeghi, I.; Ye, K.; Xu, M.; Li, Y.; LeBeau, J. M.; Jaramillo, R. Making BaZrS3 Chalcogenide Perovskite Thin Films by Molecular Beam Epitaxy. *Advanced Functional Materials* **2021**, *31*, 2105563, _eprint: https://onlinelibrary.wiley.com/doi/pdf/10.1002/adfm.202105563.

52. Misra, R. K.; Aharon, S.; Li, B.; Mogilyansky, D.; Visoly-Fisher, I.; Etgar, L.; Katz, E. A. Temperature- and Component-Dependent Degradation of Perovskite

Photovoltaic Materials under Concentrated Sunlight. *J. Phys. Chem. Lett.* **2015**, *6*, 326–330, Publisher: American Chemical Society.

53. Vaynzof, Y. The Future of Perovskite Photovoltaics—Thermal Evaporation or Solution Processing? *Advanced Energy Materials* **2020**, *10*, 2003073, _eprint: https://onlinelibrary.wiley.com/doi/pdf/10.1002/aenm.202003073.

54. Jiang, Y.; He, S.; Qiu, L.; Zhao, Y.; Qi, Y. Perovskite solar cells by vapor deposition based and assisted methods. *Applied Physics Reviews* **2022**, *9*, 021305.

55. Gil-Escrig, L.; Roß, M.; Sutter, J.; Al-Ashouri, A.; Becker, C.; Albrecht, S. Fully Vacuum-Processed Perovskite Solar Cells on Pyramidal Microtextures. *Solar RRL* **2021**, *5*, 2000553, _eprint: https://onlinelibrary.wiley.com/doi/pdf/10.1002/solr.202000553.

56. Venables, J. A.; Spiller, G. D. T.; Hanbucken, M. Nucleation and growth of thin films. *Rep. Prog. Phys.* **1984**, *47*, 399.

57. Levi, A. C.; Kotrla, M. Theory and simulation of crystal growth. *Journal of Physics: Condensed Matter* **1997**, *9*, 299.

58. Arora, N.; Greco, A.; Meloni, S.; Hinderhofer, A.; Mattoni, A.; Rothlisberger, U.; Hagenlocher, J.; Caddeo, C.; Zakeeruddin, S. M.; Schreiber, F. Kinetics and energetics of metal halide perovskite conversion reactions at the nanoscale. *Communications Materials* **2022**, *3*, 22, Publisher: Nature Publishing Group UK London.

59. Ornelas-Cruz, I.; Trejo, A.; Oviedo-Roa, R.; Salazar, F.; Carvajal, E.; Miranda, A.; Cruz-Irisson, M. DFT-based study of the bulk tin mixed-halide CsSnI3-xBrx perovskite. *Computational Materials Science* **2020**, *178*, 109619.

60. Kim, J.; Lee, S.-H.; Lee, J. H.; Hong, K.-H. The Role of Intrinsic Defects in Methylammonium Lead Iodide Perovskite. *J. Phys. Chem. Lett.* **2014**, *5*, 1312–1317, Publisher: American Chemical Society.

61. Phung, N.; Mattoni, A.; Smith, J. A.; Skroblin, D.; Köbler, H.; Choubrac, L.; Breternitz, J.; Li, J.; Unold, T.; Schorr, S.; Gollwitzer, C.; Scheblykin, I. G.; Unger, E. L.; Saliba, M.; Meloni, S.; Abate, A.; Merdasa, A. Photoprotection in metal halide perovskites by ionic defect formation. *Joule* **2022**, *6*, 2152–2174, Publisher: Elsevier.

62. Mattoni, A.; Filippetti, A.; Saba, M. I.; Delugas, P. Methylammonium Rotational Dynamics in Lead Halide Perovskite by Classical Molecular Dynamics: The Role of Temperature. *J. Phys. Chem. C* **2015**, *119*, 17421–17428, Publisher: American Chemical Society.

63. Giri, A.; Chen, A. Z.; Mattoni, A.; Aryana, K.; Zhang, D.; Hu, X.; Lee, S.-H.; Choi, J. J.; Hopkins, P. E. Ultralow Thermal Conductivity of Two-Dimensional Metal Halide Perovskites. *Nano Lett.* **2020**, *20*, 3331–3337, Publisher: American Chemical Society.

64. Li, C.; Ma, H.; Li, T.; Dai, J.; Rasel, M. A. J.; Mattoni, A.; Alatas, A.; Thomas, M. G.; Rouse, Z. W.; Shragai, A.; Baker, S. P.; Ramshaw, B. J.; Feser, J. P.; Mitzi, D. B.; Tian, Z. Remarkably Weak Anisotropy in Thermal Conductivity of Two-Dimensional Hybrid Perovskite Butylammonium Lead Iodide Crystals. *Nano Lett* **2021**, *21*, 3708–3714.

65. Mattoni, A. Molecular Rotor–Rotor Heat Diffusion at the Origin of the Enhanced Thermal Conductivity of Hybrid Perovskites at High Temperatures. **2022**, Publisher: ACS Publications.

66. Mattoni, A.; Caddeo, C. Dielectric function of hybrid perovskites at finite temperature investigated by classical molecular dynamics. *The Journal of Chemical Physics* **2020**, *152*, 104705.

67. Lehmann, A. G.; Congiu, F.; Marongiu, D.; Mura, A.; Filippetti, A.; Mattoni, A.; Saba, M.; Pegna, G.; Sarritzu, V.; Quochi, F.; Bongiovanni, G. Long-lived electrets and lack of ferroelectricity in methylammonium lead bromide CH3NH3PbBr3 fer-

roelastic single crystals. *Phys. Chem. Chem. Phys.* **2021**, *23*, 3233–3245, Publisher: The Royal Society of Chemistry.

68. Mattoni, A.; Meloni, S. Defect Dynamics in MAPbI3 Polycrystalline Films: The Trapping Effect of Grain Boundaries. *Helvetica Chimica Acta* **2020**, *103*, e2000110, _eprint: https://onlinelibrary.wiley.com/doi/pdf/10.1002/hlca.202000110.

69. Caddeo, C.; Filippetti, A.; Mattoni, A. The dominant role of surfaces in the hysteretic behavior of hybrid perovskites. *Nano Energy* **2020**, *67*, 104162.

70. Ahlawat, P.; Clementi, C.; Musil, F.; Filip, M.-A. Lattice matched heterogeneous nucleation eliminate defective buried interface in halide perovskites. 2024; `http://arxiv.org/abs/2405.11599`, arXiv:2405.11599 [cond-mat, physics:physics].

71. Ahlawat, P. Crystallization of FAPbI3: Polytypes and stacking faults. *The Journal of Chemical Physics* **2023**, *159*, 151102.

72. Mattoni, A.; Argiolas, S.; Cozzolino, G.; Dell'Angelo, D.; Filippetti, A.; Caddeo, C. Many-Body MYP2 Force-Field: Toward the Crystal Growth Modeling of Hybrid Perovskites. *J. Chem. Theory Comput.* **2024**, *20*, 6781–6789, Publisher: American Chemical Society.

73. Senftle, T. P.; Hong, S.; Islam, M. M.; Kylasa, S. B.; Zheng, Y.; Shin, Y. K.; Junkermeier, C.; Engel-Herbert, R.; Janik, M. J.; Aktulga, H. M.; Verstraelen, T.; Grama, A.; van Duin, A. C. T. The ReaxFF reactive force-field: development, applications and future directions. *npj Computational Materials* **2016**, *2*, 1–14, Publisher: Nature Publishing Group.

74. Pols, M.; van Duin, A. C. T.; Calero, S.; Tao, S. Mixing I and Br in Inorganic Perovskites: Atomistic Insights from Reactive Molecular Dynamics Simulations. *The Journal of Physical Chemistry C* **2024**, *128*, 4111–4118.

75. Pols, M.; Brouwers, V.; Calero, S.; Tao, S. How fast do defects migrate in halide perovskites: insights from on-the-fly machine-learned force fields. *Chem. Commun.* **2023**, *59*, 4660–4663.

76. Baldwin, W. J.; Liang, X.; Klarbring, J.; Dubajic, M.; Dell'Angelo, D.; Sutton, C.; Caddeo, C.; Stranks, S. D.; Mattoni, A.; Walsh, A.; Csányi, G. Dynamic Local Structure in Caesium Lead Iodide: Spatial Correlation and Transient Domains. *Small* **2024**, *20*, 2303565.

77. Sloane, N. P.; Bailey, C. G.; Cole, J. H.; Schmidt, T. W.; McCamey, D. R.; Klymenko, M. V. Electronic Structure at the Perovskite/Rubrene Interface: The Effect of Surface Termination. *The Journal of Physical Chemistry C* **2024**,

78. Lu, Y.; Zhixiang, S.; Liu, H.; Ge, Y.; Hu, J.; Zhang, Z.; Mu, X.; Selvakumar, K.; Sui, M. In CH3NH3PbI3 Perovskite Film, the Surface Termination Layer Dominates the Moisture Degradation Pathway. *Chemistry: A European Journal* **2021**, *27*, 3729–3736.

79. Du, Z.; Ma, Z.; Yu, T.; Huang, Z.; You, W.; Chen, Y.; Yang, J.; Du, H.; Zhang, Q.; Li, Y.; Bai, L.; Li, Y.; Li, G.; Hou, S.; Xiang, Y.; Yu, J.; Huang, C.; Sun, K.; Long, W. Regulation of Lead Iodide Crystallization and Distribution for Efficient Perovskite Solar Cells. *ACS Applied Materials & Interfaces* **2024**, *16*, 49584–49593.

80. Liu, Y.; Zhang, X.; Song, B.; Chen, X.; Wei, F.; Yuan, J.; Shen, B. Atomic Imaging of the Pb Precipitation in Lead-Halide Perovskites. *Small methods* **2024**, e2301617–e2301617.

81. Mallick, A.; Visoly-Fisher, I. Pb in halide perovskites for photovoltaics: reasons for optimism. *Materials Advances* **2021**, *2*, 6125–6135.

82. Mattoni, A.; Colombo, L. Crystallization kinetics of mixed amorphous-crystalline nanosystems. *Phys. Rev. B* **2008**, *78*, 075408.

83. Mattoni, A.; Colombo, L. Nonuniform Growth of Embedded Silicon Nanocrystals in an Amorphous Matrix. *Phys. Rev. Lett.* **2007**, *99*, 205501.

84. Fugallo, G.; Mattoni, A. Thermally induced recrystallization of textured hydrogenated nanocrystalline silicon. *Phys. Rev. B* **2014**, *89*, 045301.

85. Shargaieva, O.; Näsström, H.; Li, J.; Többens, D. M.; Unger, E. L. Temperature-Dependent Crystallization Mechanisms of Methylammonium Lead Iodide Perovskite From Different Solvents. *Front. Energy Res.* **2021**, *9*, Publisher: Frontiers.

86. Meggiolaro, D.; Mosconi, E.; De Angelis, F. Formation of Surface Defects Dominates Ion Migration in Lead-Halide Perovskites. *ACS Energy Lett.* **2019**, *4*, 779–785, Publisher: American Chemical Society.

87. Li, B.; Kan, C.; Hang, P.; Fang, Y.; Zuo, L.; Song, L.; Zhang, Y.; Yang, D.; Yu, X. Understanding the Influence of Cation and Anion Migration on Mixed-Composition Perovskite Solar Cells via Transient Ion Drift. *physica status solidi (RRL) – Rapid Research Letters* **2021**, *15*, 2100225, _eprint: https://onlinelibrary.wiley.com/doi/pdf/10.1002/pssr.202100225.

88. Di Girolamo, D.; Phung, N.; Kosasih, F. U.; Di Giacomo, F.; Matteocci, F.; Smith, J. A.; Flatken, M. A.; Köbler, H.; Turren Cruz, S. H.; Mattoni, A.; Cinà, L.; Rech, B.; Latini, A.; Divitini, G.; Ducati, C.; Di Carlo, A.; Dini, D.; Abate, A. Ion Migration-Induced Amorphization and Phase Segregation as a Degradation Mechanism in Planar Perovskite Solar Cells. *Advanced Energy Materials* **2020**, *10*, 2000310, _eprint: https://onlinelibrary.wiley.com/doi/pdf/10.1002/aenm.202000310.

89. M. Azpiroz, J.; Mosconi, E.; Bisquert, J.; Angelis, F. D. Defect migration in methylammonium lead iodide and its role in perovskite solar cell operation. *Energy & Environmental Science* **2015**, *8*, 2118–2127, Publisher: Royal Society of Chemistry.

90. Delugas, P.; Caddeo, C.; Filippetti, A.; Mattoni, A. Thermally Activated Point Defect Diffusion in Methylammonium Lead Trihalide: Anisotropic and Ultrahigh Mobility of Iodine. *J. Phys. Chem. Lett.* **2016**, *7*, 2356–2361, Publisher: American Chemical Society.

91. Keeble, D. J.; Wiktor, J.; Pathak, S. K.; Phillips, L. J.; Dickmann, M.; Durose, K.;

Snaith, H. J.; Egger, W. Identification of lead vacancy defects in lead halide perovskites. *Nat Commun* **2021**, *12*, 5566, Publisher: Nature Publishing Group.

92. Ambrosio, F.; Meggiolaro, D.; Mosconi, E.; Angelis, F. D. Charge localization and trapping at surfaces in lead-iodide perovskites: the role of polarons and defects. *J. Mater. Chem. A* **2020**, *8*, 6882–6892, Publisher: The Royal Society of Chemistry.

93. Meggiolaro, D.; De Angelis, F. First-Principles Modeling of Defects in Lead Halide Perovskites: Best Practices and Open Issues. *ACS Energy Lett.* **2018**, *3*, 2206–2222, Publisher: American Chemical Society.

94. Delugas, P.; Filippetti, A.; Mattoni, A. Methylammonium fragmentation in amines as source of localized trap levels and the healing role of Cl in hybrid lead-iodide perovskites. *Phys. Rev. B* **2015**, *92*, 045301, Publisher: American Physical Society.

95. Park, B.-w.; Seok, S. I. Intrinsic Instability of Inorganic–Organic Hybrid Halide Perovskite Materials. *Advanced Materials* **2019**, *31*, 1805337, _eprint: https://onlinelibrary.wiley.com/doi/pdf/10.1002/adma.201805337.

96. Xue, H.; Vicent-Luna, J. M.; Tao, S.; Brocks, G. Compound Defects in Halide Perovskites: A First-Principles Study of CsPbI3. *J. Phy. Chem. C* **2023**, *127*, 1189–1197.

97. Ponder, J. W.; Case, D. A. Force fields for protein simulations. *Adv Protein Chem* **2003**, *66*, 27–85.

98. Matsui, M. Molecular dynamics study of MgSiO3 perovskite. *Physics and Chemistry of Minerals* **1988**, *16*, 234–238, ADS Bibcode: 1988PCM....16..234M.

99. Liu, Z.-J.; Zhang, C.-R.; Sun, X.-W.; Hu, J.-B.; Song, T.; Chu, Y.-D. The melting curve of MgSiO3 perovskite from molecular dynamics simulation. *Phys. Scr.* **2011**, *83*, 045602.

100. Thompson, A. P.; Aktulga, H. M.; Berger, R.; Bolintineanu, D. S.; Brown, W. M.; Crozier, P. S.; in 't Veld, P. J.; Kohlmeyer, A.; Moore, S. G.; Nguyen, T. D.;

Shan, R.; Stevens, M. J.; Tranchida, J.; Trott, C.; Plimpton, S. J. LAMMPS - a flexible simulation tool for particle-based materials modeling at the atomic, meso, and continuum scales. *Comp. Phys. Comm.* **2022**, *271*, 108171.

101. Giannozzi, P.; Baroni, S.; Bonini, N.; Calandra, M.; Car, R.; Cavazzoni, C.; Ceresoli, D.; Chiarotti, G. L.; Cococcioni, M.; Dabo, I.; Corso, A. D.; Gironcoli, S. d.; Fabris, S.; Fratesi, G.; Gebauer, R.; Gerstmann, U.; Gougoussis, C.; Kokalj, A.; Lazzeri, M.; Martin-Samos, L. *et al.* QUANTUM ESPRESSO: a modular and open-source software project for quantum simulations of materials. *Journal of Physics: Condensed Matter* **2009**, *21*, 395502.

102. Giannozzi, P.; Andreussi, O.; Brumme, T.; Bunau, O.; Buongiorno Nardelli, M.; Calandra, M.; Car, R.; Cavazzoni, C.; Ceresoli, D.; Cococcioni, M.; Colonna, N.; Carnimeo, I.; Dal Corso, A.; de Gironcoli, S.; Delugas, P.; DiStasio, R. A.; Ferretti, A.; Floris, A.; Fratesi, G.; Fugallo, G. *et al.* Advanced capabilities for materials modelling with Quantum ESPRESSO. *Journal of Physics: Condensed Matter* **2017**, *29*, 465901.

103. Perdew, J. P.; Burke, K.; Ernzerhof, M. Generalized Gradient Approximation Made Simple. *Phys. Rev. Lett.* **1996**, *77*, 3865–3868, Publisher: American Physical Society.

104. Jollet, F.; Torrent, M.; Holzwarth, N. Generation of Projector Augmented-Wave atomic data: A 71 element validated table in the XML format. *Computer Physics Communications* **2014**, *185*, 1246–1254.

105. Humphrey, W.; Dalke, A.; Schulten, K. VMD – Visual Molecular Dynamics. *Journal of Molecular Graphics* **1996**, *14*, 33–38.

106. Williams, T.; Kelley, C.; many others Gnuplot 4.6: an interactive plotting program. `http://gnuplot.sourceforge.net/`, 2013.

TOC Graphic

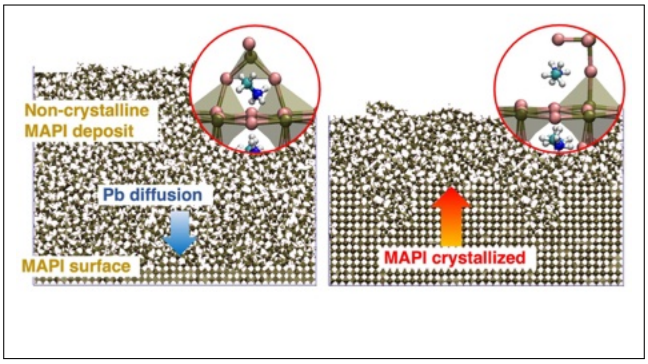
Non-crystalline
MAPI deposit
Pb diffusion
MAPI surface
MAPI crystallized